FISEVIER

Contents lists available at ScienceDirect

Journal of Materials Research and Technology

journal homepage: www.elsevier.com/locate/jmrt





Influence of melt parameters on the microstructure of electron beam melted Ti-6Al-4V

G.R. Davies ^a, R.J. Lancaster ^a, M. Thomas ^{b,*}, I. Todd ^c, D. Stapleton ^d, G.J. Baxter ^{c,d}

- a Institute of Structural Materials, Bay Campus, Swansea University, Swansea, SA1 8EN, United Kingdom
- ^b Interdisciplinary Programmes in Engineering, University of Sheffield, Sheffield, S1 3JD, United Kingdom
- ^c Department of Materials Science & Engineering, The University of Sheffield, Mappin Street, Sheffield, S1 3JD, United Kingdom
- ^d Rolls-Royce Plc, Derby, DE24 8EG, United Kingdom

ARTICLE INFO

Handling editor: L Murr

Keywords: Ti-6Al-4V Electron beam melting Process parameters Microstructure

ABSTRACT

Additively manufactured, Electron Beam Melted (EBM) specimens of the titanium alloy, Ti–6Al–4V, have been produced using a process window determined through a normalised energy density method. Two batches were manufactured and compared using identical energy density values with differing beam current, power, and beam velocity. A stable process window has been demonstrated with a Vickers hardness range of 360–395 VHN resulting from α lath coarsening from 0.7 μ m up to 3 μ m. A range of macro morphologies have been reported and relate to the hatch overlap and beam velocity parameters. Base plate position does not appear to influence microstructure or micro-hardness. Prior- β columnar and colony size increases with α lath width resulting from increased energy input; however, each grain type appears to respond differently to either beam velocity or hatch space variation. Average α lath width values show greater correlation to energy density, which demonstrates the dependence of grain formation on hatch overlap.

1. Introduction

Additive Manufacturing (AM) is a process in which digital 3D design data is directly employed to build a component in a layer-wise method. The strengths and benefits of AM lie in the areas where subtractive manufacturing nears its limits. AM builds up components in sequential layers from feedstock material such as that available in fine powder form. The technology is now of significant interest to a considerable number of industrial sectors who are looking for innovative approaches to design and manufacture intricately complex components. Furthermore, it provides a high degree of design freedom for engineers and the optimisation and integration of functional features which would not have been possible using subtractive manufacturing alone.

Electron Beam Melting (EBM) is one of the prominent AM techniques adopted by the aerospace and medical industries. The fundamental principle of EBM is the selective melting of discrete powder layers by an electron beam under vacuum conditions. The electron beam is emitted from a tungsten filament which is controlled by two magnetic coils for focusing and controlling the position and speed of the beam. This allows for multiple melt pools to be maintained, which can increase productivity. In addition to beam power, several other manufacturing process

variables, including beam velocity, hatch spacing, layer height and energy density, also have a key influence on the variability and integrity of the finished part. Extensive reviews of the microstructure and mechanical properties of Ti–6Al–4V fabricated by EBM [1] and other additive manufacturing technologies [2] are available in the literature and much of the background information on the relationship between processing, microstructure and properties is covered in these articles.

Line energy (J/m) is proportional to power, inversely proportional to beam velocity and is delivered to the powder along a single melt line [3, 4]. Korner et al. [5] demonstrated that low line energy caused discontinuous patches of molten powder whilst higher line energy increased the size of the droplets until a solidified surface was formed. Maintaining constant line energy through changing velocity and compensating with increased beam power was shown, through experimentation, to dominate the final weld track macrostructure. Simulations with constant powder packing factors revealed that, in terms of process variables, the line energy was the most dominant [5]. Korner et al. [5] devised a process map demonstrating observations such as the balling effect. A combination of higher beam power and lower scan speed were shown to produce continuous melt tracks with sufficient melt penetration. Juechter et al. [3] considered line energy comparisons with scanning

E-mail address: Meurig.thomas@sheffield.ac.uk (M. Thomas).

^{*} Corresponding author.

speed. Lower line energy values were attributed to porosity formations at the specimen surface. As line energy increased, the morphology was shown to change from porous looking structures to uneven structures caused by part swelling [3,6]. Morita et al. [7] conducted studies into the scan speed effects in EBM. Faster scan speeds were found to increase the population of features from small pores to lack of fusion (LOF). This corresponded with greater geometric accuracy, increased hardness and increases in martensite content. For the parameters chosen, internal imperfections were almost completely removed at 0.5 m/s. Narra et al. [8] considered the effect of parameters with prior-β grain size to find a power law decay with speed function. Increasing the speed function caused the melt pool area to increase whilst a reduction in the speed function caused grain size increase. Kirchner et al. [9] manipulated beam current and velocity by determining the line energy. Material density was shown to reduce progressively with increasing scan speed. A similar trend was seen with beam current. Higher beam speeds led to the formation of $\alpha^{\boldsymbol{\cdot}}$ which was still found to be present even at temperatures around 700 °C.

Thomas et al. [10] outlined a series of normalised process parameters collated from a range of literature sources. By normalising the input parameters, a range of parameters was compiled into one normalised-based process parameter map. The dimensionless beam power (q^*) , velocity (v^*) and layer height (l^*) were used to calculate the normalised volumetric energy density (E^*) :

$$E^* = \frac{q^*}{\nu^* l^*} = \left[\frac{Aq}{2\nu l r_B}\right] \left[\frac{1}{\rho C_p(T_m - T_0)}\right]$$
 Eq. 1

Where A is the coupling coefficient (or surface absorptivity) and $r_{\rm B}$ is the radius of the moving heat source (in this case an electron beam). The terms ρ , $C_{\rm p}$ and $T_{\rm m}$ refer to the density, specific heat capacity and melting temperature of the engineering alloy being treated, whilst the terms q, v, l and $T_{\rm 0}$ correspond to the heat source power, heat source velocity, powder bed layer height and the initial temperature of the powder bed, respectively. The hatch spacing (h) was normalised against the beam radius $r_{\rm B}$ to give the following dimensionless hatch spacing (h^*):

$$h^* = \frac{h}{r_B}$$
 Eq. 2

Equations (1) and (2) were combined to give the normalised equivalent energy density, E_0^* :

$$E_0^* = \frac{q^*}{\nu^* l^* h^*}$$
 Eq. 3

The notion was that across different AM platforms and alloys, there exists a process window within which a desirable combination of processing parameters will produce a desirable build quality. This method acted to unify a range of parameters and identify suitable combinations of those from within an initial window of values, thus avoiding defective or undesirable build results. The map was then able to correlate similarities between different AM processes and different alloy types by factoring in a range of material specific constants with AM process parameters, as depicted in Fig. 1. The aim of this paper is to directly correlate the microstructure of EBM Ti–6Al–4V to some of the fundamental processing parameters in the form of normalised energy density by assessing what has been considered and predicted to be an acceptable process window for this alloy.

2. Experimental methods

The material produced and assessed for this project was deposited sing an Arcam S12 EBM machine system at the University of Sheffield using a gas atomised Ti–6Al–4V powder with a nominal particle size distribution (PSD) of 45–105 $\mu m.$ A total of eleven cubes of nominally 15 x 15 \times 15 mm were manufactured a minimum of 10 mm away from any given neighbour on the build plate. All specimens were built

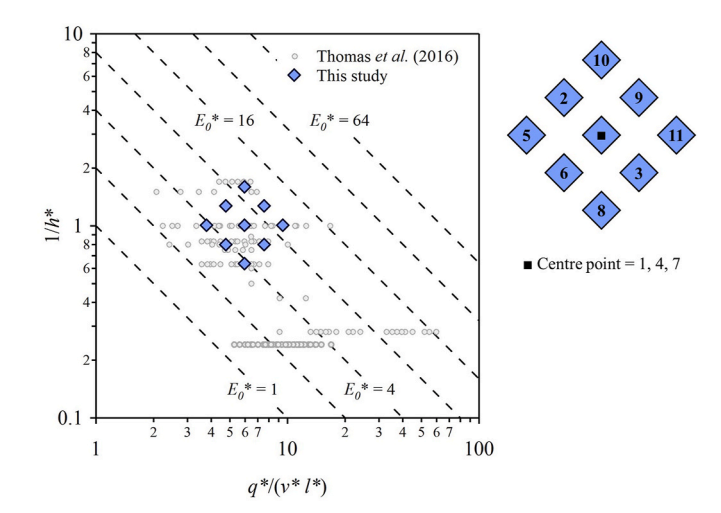


Fig. 1. Process window map with the current Design of Experiment (DoE) parameters for this research superimposed on the data from Thomas et al. [10]. The corresponding position in processing space of each of the specimen numbers listed in Table 1 are also indicated on the right-hand side.

immediately onto the base plate without the use of supports. The selected EBM processing parameters were based upon a central composite design of experiments (DoE) and the standard EBM melt themes were disengaged in favour of manual parameter combinations. For each sample produced, the power (q) and layer height (l) were kept constant, and the variation in dimensionless energy density (E_0^*) achieved by controlling only the beam velocity (v) and hatch spacing (h). In combination, the parameters were equal to the normalised energy density values within the processing diagram shown in Fig. 1, which contains the data reported in a previous study [10] as well as the proposed DoE parameters for this experiment. The thermophysical property data used to calculate the dimensionless processing variables in Equations (1)–(3) are listed in Table 1.

The EBM processing parameters investigated in this study are listed in Table 2. Each specimen reference number correlates to a given set of processing parameter combinations and, therefore, location on the normalised processing diagram (Fig. 1). The physical position of the specimens on the build base plate was randomised. The eleven samples represent a total of nine processing parameter combinations, where three samples; 1, 4 and 7, represent a replicate of a parameter set ($E^* = 6.03$ and $h^* = 1$) and therefore lie in the same location on the processing diagram. Except in the case of the replicate parameter set, the effect of the base plate position has not been investigated.

The microstructures of the cubes were characterised using a Reichert Jung MeF3 optical microscope and a Zeiss EvoLS25 Scanning Electron Microscope (SEM) with Electron Back Scatter Diffraction (EBSD). For EBSD analysis, a step size of 0.25 μm was used alongside HKL Channel 5's post processing software. α lath width measurements of the acicular microstructure were manually measured using ImageJ perpendicular to the grain orientation. Specimens were prepared using a standard polishing technique for titanium alloys and all lath measurements were manually measured on specimens etched using a Kroll's reagent (2% hydrofluoric acid in H_2O).

Table 1The thermophysical property data for Ti–6Al–4V used to calculate the dimensionless processing parameters in Equations (1)–(3). Thermophysical property data taken from Ref. [10].

Melting temperature, T_m	Specific heat capacity, C_p	Density, ρ	Thermal conductivity, λ	Thermal diffusivity, α
1988 K	$621~{ m J~kg^{-1}} \ { m K^{-1}}$	4378 kg m ⁻³	$15.75~W~m^{-1}$ K^{-1}	5.79E-6 m ² s ⁻¹

Table 2 The Electron Beam Melting (EBM) processing parameters investigated in this study. Beam power = q; beam velocity = v, layer height = l and hatch spacing = h. The corresponding dimensionless values are denoted by an *. Replicates are indicated by a †.

Specimen number	q	q*	v	v*	1	1*	h	<u>h*</u>	q*/(v*l*)	1/(h*)	q*/(v*.l*.h*)
	(W)	(-)	(m/s)	(-)	(m)	(-)	(m)	(-)	(-)	(-)	(-)
1 †	300	35.77	0.49	12.72	7.00E-05	0.47	1.50E-04	1.00	6.03	1.00	6.03
2	300	35.77	0.62	16.01	7.00E-05	0.47	1.19E-04	0.79	4.79	1.26	6.03
3	300	35.77	0.39	10.10	7.00E-05	0.47	1.89E-04	1.26	7.59	0.79	6.03
4 †	300	35.77	0.49	12.72	7.00E-05	0.47	1.50E-04	1.00	6.03	1.00	6.03
5	300	35.77	0.78	20.16	7.00E-05	0.47	1.50E-04	1.00	3.80	1.00	3.80
6	300	35.77	0.62	16.01	7.00E-05	0.47	1.89E-04	1.26	4.79	0.79	3.80
7 †	300	35.77	0.49	12.72	7.00E-05	0.47	1.50E-04	1.00	6.03	1.00	6.03
8	300	35.77	0.49	12.72	7.00E-05	0.47	2.38E-04	1.58	6.03	0.63	3.80
9	300	35.77	0.39	10.10	7.00E-05	0.47	1.19E-04	0.79	7.59	1.26	9.55
10	300	35.77	0.49	12.72	7.00E-05	0.47	9.46E-05	0.63	6.03	1.58	9.55
11	300	35.77	0.31	8.03	7.00E-05	0.47	1.50E-04	1.00	9.55	1.00	9.55
Beam radius, r_B		1.5E-4 m	Surface a	bsorptivity, A	0.6	Bed ten	nperature, T_0	923 K	Layer height	, 1	7.0E-5 m

Hardness values were recorded using an Innovatest Nexus 4000 series Vickers hardness tester under a 1 kg load over a 10 s dwell period. In all cases, unless stated, a minimum of nine indents were made and a mean average hardness calculated.

3. Results and discussion

Fig. 2 shows the comparison between light micrographs and SEM of

the replicate parameter set. Virtually no difference in microstructure was observed in the replicate specimens, demonstrating that position of build on the base plate has little or no effect on the resulting microstructure. All samples have basketweave, Widmanstätten colony microstructures, a reduced prior- β columnar width, as well as allotriomorphic grain boundary α types (Fig. 2 b), d) and f)). The refined basketweave morphology is indicative of low energy specimens such as lath structures developed in cold bed processes [2,11,12] and in EBM

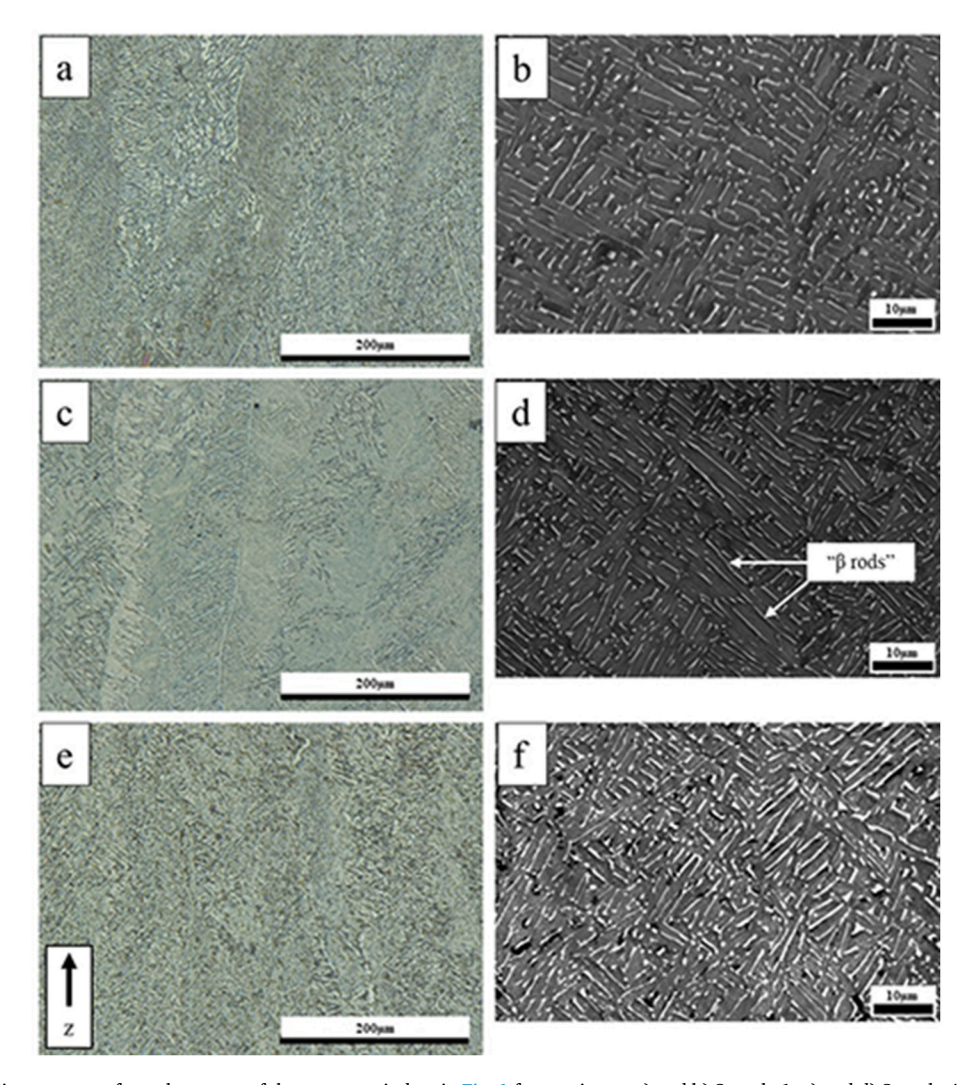


Fig. 2. Comparison of microstructure from the centre of the process window in Fig. 1 for specimens a) and b) Sample 1, c) and d) Sample 4, e) and f) Sample 7. $E_0^* = 6.03$ for all cases. The build direction, (z) is vertical in all cases.

technologies using comparable process parameters (see for example Fig. 2 a) and b) in Ref. [13]).

The effect of normalised volumetric energy density (E^*) and dimensionless hatch spacing (h^*) on the microstructure of AM Ti–6Al–4V is shown in Figs. 3 and 4. Higher energy densities resulted in microstructures with predominantly more colonies and coarser laths forming into Widmanstätten structures. This is seen at both length scales using optical and SEM imaging. Smaller grained specimens, shown in Fig. 3 a), c), e) and g), can be defined not only in terms of lath width and morphology but also β enriched zones or ' β ' rods which become less interrupted as the energy increases (Fig. 4). In addition, the morphology of the structure changes from basketweave to an angular Widmanstätten

formation whilst increasing the number of parallel laths formed by arrays of angled colonies that are woven together. At lower energy levels, the Widmanstätten type morphology often includes singular lath formations per direction with broken β rod formations. It is clear from the images that lower energy density conditions produce much higher proportions of β -islands and straighter rod formations. At higher energy densities, the β rods become slightly more tortuous, and the island structures virtually disappear (Fig. 4 f) and h)).

Each of the morphological types (α lath width, colony size and prior- β colony width) were measured and compared with the normalised equivalent energy density (E_0^*), and these are summarised in Fig. 5. In all cases, increasing E_0^* lead to a commensurate coarsening of the

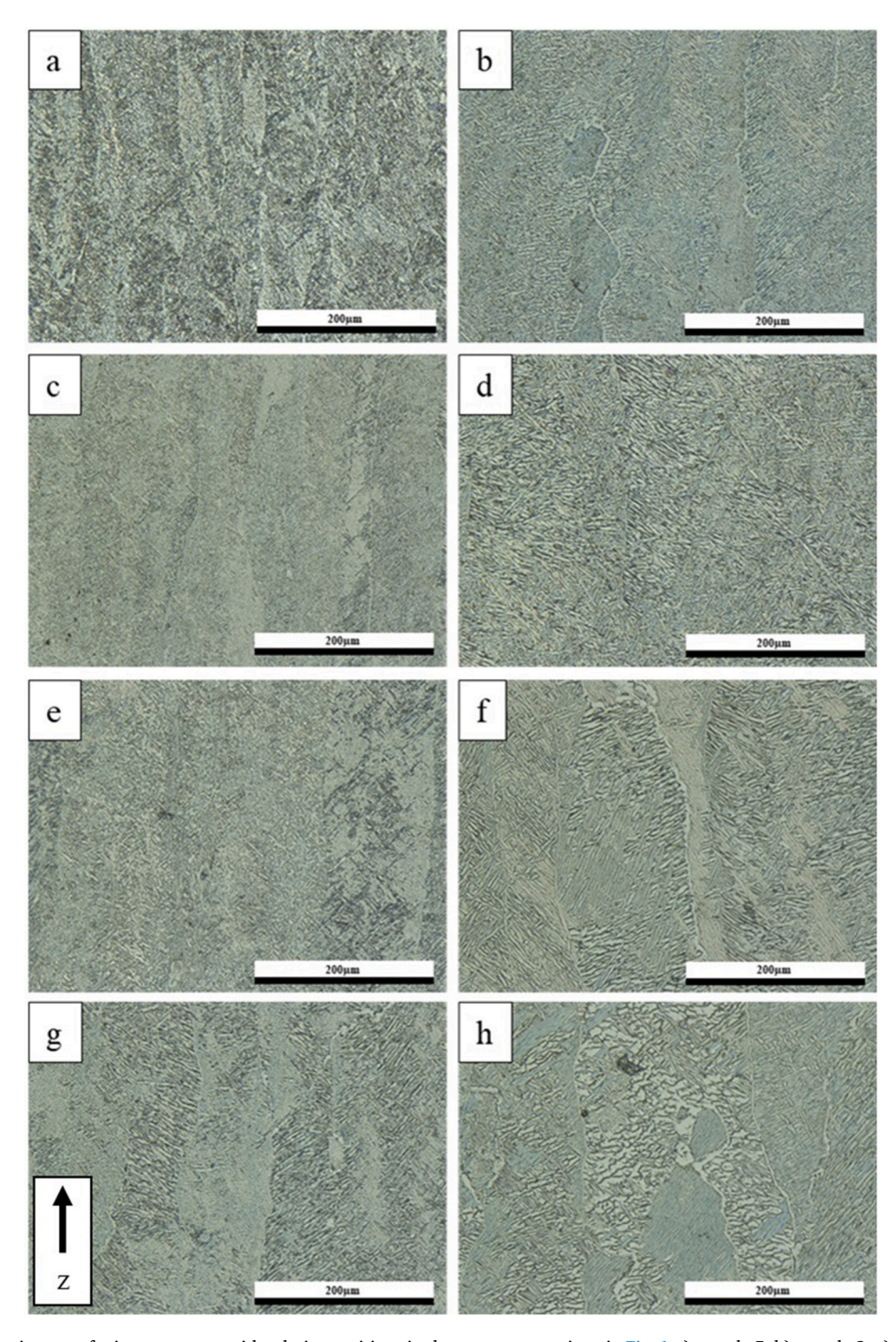


Fig. 3. Optical microscopy images of microstructures with relative positions in the process map given in Fig. 1 a) sample 5, b) sample 2, c) sample 6, d) sample 10, e) sample 8, f) sample 9, g) sample 3, h) sample 11. The build direction, (z) is vertical in all cases.

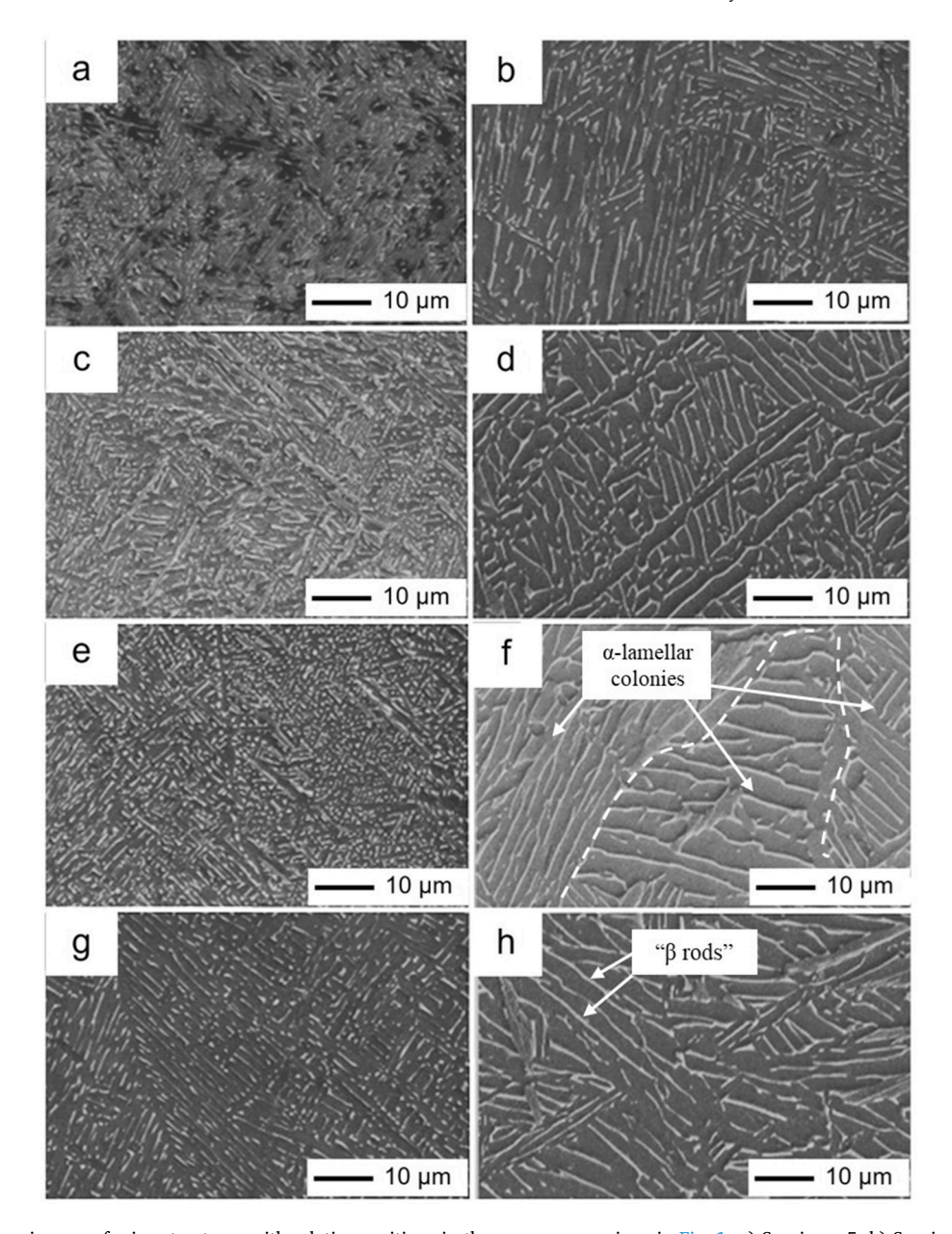


Fig. 4. Scanning electron images of microstructures with relative positions in the process map given in Fig. 1; a) Specimen 5; b) Specimen 2; c) Specimen 6; d) Specimen 10; e) Specimen 8; f) Specimen 9; g) Specimen 11.

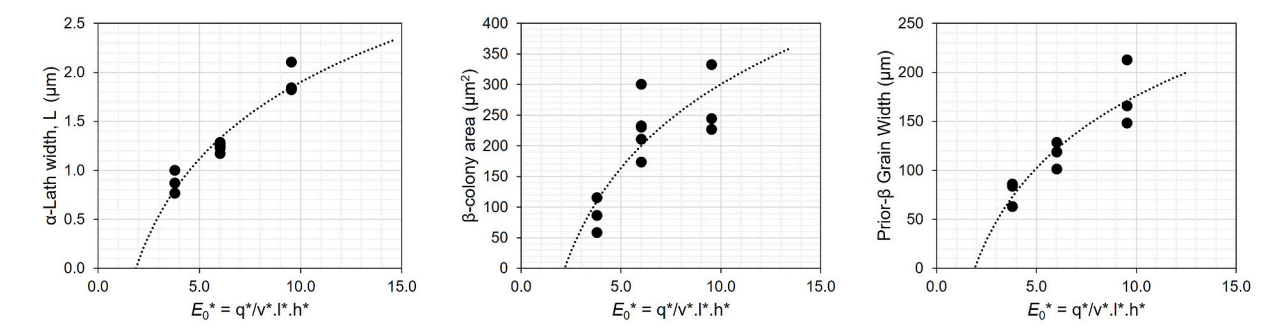


Fig. 5. Scatter plots showing the variation in a) α -lath width, b) β -colony area and c) prior- β columnar grain width as a function of dimensionless equivalent energy density, E_0^* .

microstructural unit size and an interesting relationship has arisen relating grain coarsening to the energy density. Fig. 5 a) compares the α lath width with E_0^* as an example chosen to represent the type of trend line used to describe microstructural unit size as a function of normalised energy density. Applying a linear trend would suggest that an ultrafine grain type throughout the energy scale could be achieved and would be demonstrated at higher magnification. However, the morphology does appear to differ throughout the images shown in Figs. 3 and 4. The lower energy density ultimately produces a higher proportion of discontinuous β -rods at the lath boundary which become far more continuous in the microstructure of the higher energy density specimens. Secondly, the natural linear trend-line for the data presented for all morphological types leads to an intercept of the vertical y axis at a lath width value which is positive where the energy density is equal to zero suggesting that a microstructure could be developed without any energy input. For these two reasons, the linear fit has been discounted and the logarithmic curve has been adopted. A logarithmic curve suggests a degree of diminishing returns as the *x* axis value increases. This would be satisfied, as the onset of excessive swelling (if allowed to continue) would ultimately lead to a failed build or key-holing at higher energy inputs. Therefore, it can be presumed that there is a given theoretical maximum governed by a practical limit such as excessive swelling. Observations of Fig. 5 show that in each case where both the normalised beam speed and hatch offset are considered, the intercept of the trend-line across the horizontal x axis falls into the same approximate value. This suggests that a critical value for E_0 * exists for the microstructural development of EBM Ti-6Al-4V. It is predicted from this fit that colony size, lath width and columnar grain growth will begin in regions where $E_0*_{\min} \approx 2$ is satisfied, although this may be a conservative estimate and this value may in practicality be larger. What this trend does demonstrate however, is the potential for the grains to undergo a proportionally larger degree of growth at the lower energy levels, which would stabilise throughout the range and then ultimately diminishing with increasing energy input.

The specimens that were subjected to the highest and lowest beam speeds (sample 11 and sample 5), but with equal hatch offset, underwent further analysis to determine the size distribution of the α -lath width between the two. Samples 5 and 11 represent the lowest and highest values of the E^* and E_0^* parameters and fall on the left- and right-hand side of the processing diagram in Fig. 1. The corresponding microstructures are presented in Fig. 4 a) and h). To determine the characteristics of the α -lath sizes, a series of 10,000 manual measurements

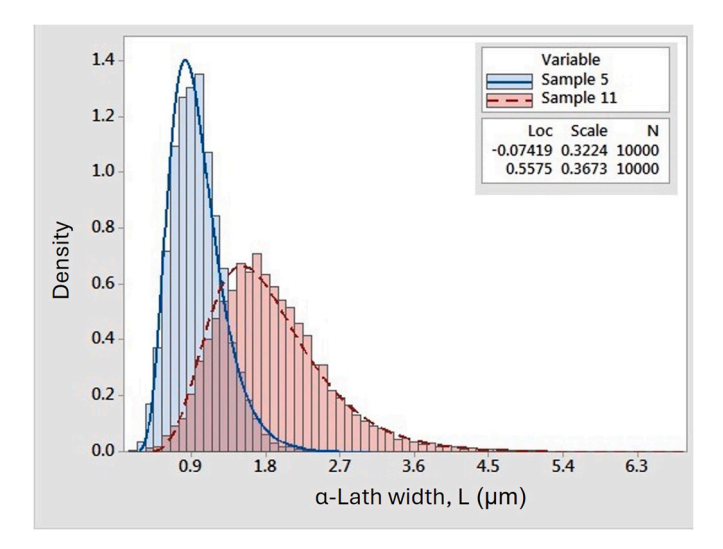


Fig. 6. Comparative distribution of the measured α-lath widths across the 10,000 measurements for Specimen 5 ($E_0^* = 3.80$) and Specimen 11 ($E_0^* = 9.55$). Data points represent the mean average values from 100 images.

were taken on each specimen, corresponding to 100 measurements taken from 100 secondary electron images taken at ×1000 magnification (Fig. 6). The mean α lath width for sample 5 was 0.97 μm and the standard deviation was 0.305 µm. In comparison, a higher energy density (sample 11) results in an α -lath size distribution that is broader with a mean average of 1.86 μm and a standard deviation of 0.41 μm between images, increasing to 0.7 µm across all the images measured. The results show that the lath size development from the lower to the higher energy density conform well to a log-normal distribution. Vickers microhardness measurements were performed on all eleven of the samples investigated in this study and the data is presented in the form of a Hall-Petch plot in Fig. 7. The Vickers hardness data collected in this study falls in the range 360-395 VHN and the relationship between VHN and the inverse square root of the α lath width aligns closely with that reported by Thomas et al. [10] (open circles in Fig. 7). The relationship between hardness and microstructural unit size can be described by a modified Hall-Petch relationship:

$$H_0 = H_i + \frac{k}{L^{1/2}}$$
 Eq. 4

where H_0 is the Vickers hardness number (VHN) and L is the α lath width. A linear regression analysis was performed on all the data presented in Fig. 7 and the Hall-Petch constants k and H_i in Equation (4) were determined to be 93.3 \pm 11.8 μ m^{1/2} and 287.2 \pm 8.3 VHN (95% confidence interval), respectively.

Crystallographic texture data for samples 5 and 11 are presented in Fig. 8. The EBSD maps show that the maximum multiples of uniform density (MUD) differ between 18.96 and 50.99 between the lower (sample 5) and higher (sample 11) energy density specimens respectively. However, this concentration may differ over larger scan areas. Lath structures in the lower energy density specimens have a greater aspect ratio and, in some cases, can be seen to extend across the span of each of the columnar grains. Overall, the IPF (Z) map shows pink coloured grains are predominantly most present (with planes half-way rotated between [0001] and [01–10]). This is also shown to be the most common orientation for the grain boundary α seen to the left-hand

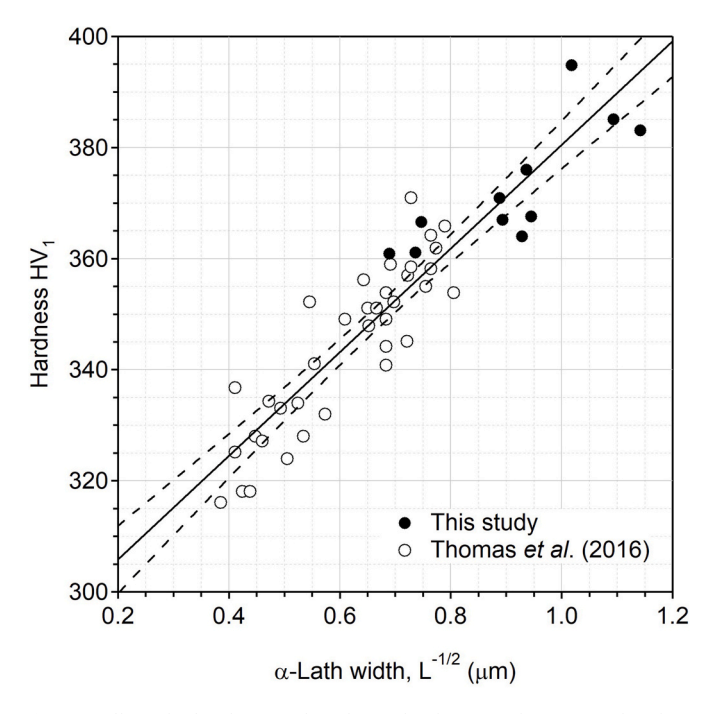


Fig. 7. Hall-Petch plot showing the relationship between the measured Vickers Hardness Number and the inverse square root of the α lath width, $L^{-1/2}$. Vickers hardness data from this study is compared with data for Additively Manufactured Ti–6Al–4V from Thomas et al. (2016) [10].

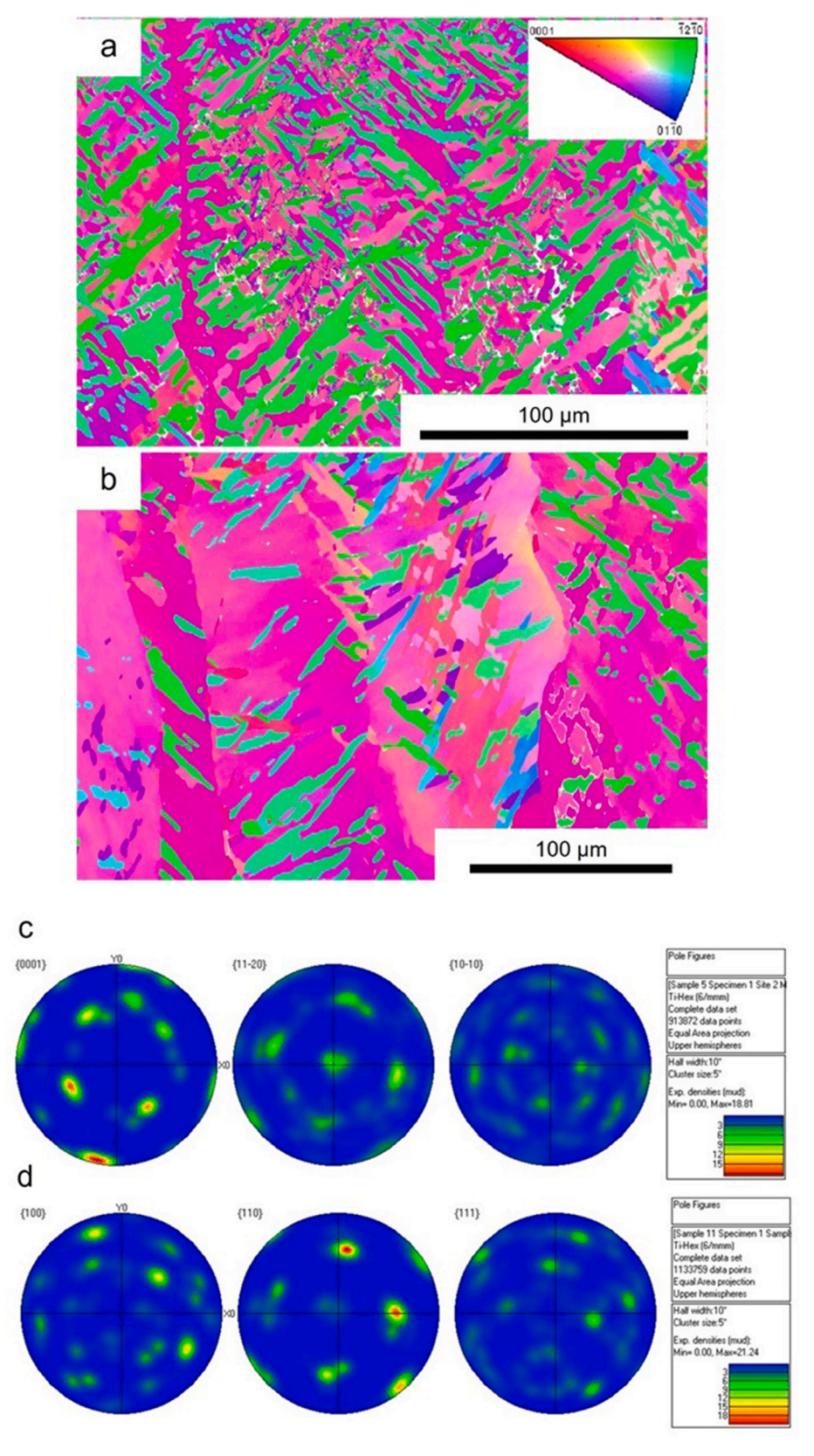


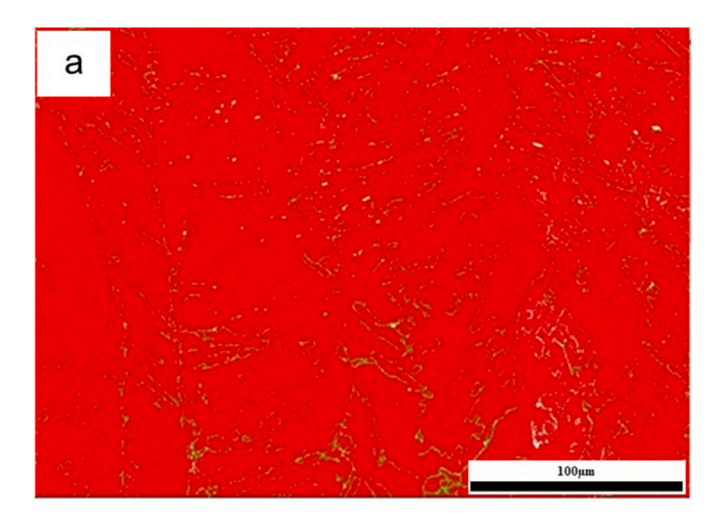
Fig. 8. EBSD results of a) Sample 5 Inverse Pole Figure (Z) map, b) Sample 11 Inverse Pole Figure (Z) map, c) Sample 5 pole figure for the data set and d) Sample 11 pole figure for the data set. Sample 5 is the low normalised energy density specimen ($E_0^* = 3.80$), whilst Sample 11 is the high energy density specimen ($E_0^* = 9.55$).

side of the image, running from the top of the map to the bottom. This orientation is regularly intersected by [-12-10] orientated α laths. Such laths are seen traversing across the entire map where some examples are almost perfectly in-line with each other across multiple prior- β boundaries. This is not to say that the laths originate from the same source but that such features are found across adjacent columnar grains.

Structures in the higher energy density show a similar overall pink coloured texture (with planes half-way rotated between [0001] and [01–10]), also intersected by α laths with planes commonly orientated to [-12-10]. Clear differences in overall texture are seen between the two specimens. Across certain locations, little difference in orientation is seen across the entire map showing that adjacent columnar structures have developed in a very similar manner. Swathes of regions form into colonies which in turn form almost the entirety of the width of the columns. Intersections of the prior- β columnar grains by α laths orientated differently do not seem to translate across the same spans as with the lower energy density. Such laths in this case have different aspect ratios to the lower energy densities. In both cases it is not always clear from the IPF maps as to whether they constitute individual laths. However, in certain locations there are multiple laths forming in parallel and the intersecting [-12-10] orientated laths are likely to be colonies. Nevertheless, the density and frequency of such intersecting structures diminishes, and it appears that changes in spatial or geometric lath orientations producing the basketweave type structures are lost. The higher energy input has seemingly amalgamated the crosshatching structures and produced laths which are far more geometrically aligned into larger colonies. Pole figures between both samples remain consistent and in-line with those produced previously [14,15] differing only in terms of MUD values, which suggest that specific regions only differ in concentration compared with a larger area.

Grain sizes begin to shift upwards of 25 μm , for the smaller grain variant, and 130 μm , for the larger grain material. For a purely basketweave structure it may be expected that the individual laths which are oriented separately may be classed as an individually definable 'grain'. However, when alignment begins to occur, laths develop in parallel and take on similar crystallographic orientations. This shifts the calculation as the energy density increases. The texture produced causes the EBSD software to identify effective structural units (ESU) as single grains, similar to the work of Sackett et al. [16]. When comparing this with manual lath measurements it is clear that a more suitable comparison can be made and the effective unit size tends towards the colony size. Local variations in macro texture may contribute to the greater variation in microhardness.

The distribution of the local misorientation (Fig. 9) in both cases seems to concentrate around the lath boundaries. Such concentrations are seen to a greater degree where the energy density is low (Fig. 9 a)). The contrasting images show that local misorientation is comparatively greater for the higher energy density specimen, sample 11 (Fig. 9 b)). The comparison of the misorientation maps has highlighted that the indexing rate of the material is improved as the energy density increases. Here, the non-indexed regions of the map appear to be concentrated around the colony boundary rather than the lath boundaries. This behaviour has been found previously in the literature where local misorientation has been shown to act as a precursor for detecting crack growth due to the correlation with plastic strain and local misorientation where mapping of the inter grain misorientation has been used to show deformation fields; the inter grain strain in this case resulted from plastic deformation [17]. Salvati et al. [18] used the misorientation within the grains to indicate plastic strain distribution near the tip of the crack by utilising the intra granular deformation gradients as evidence of the presence of dislocation pileup near the grain boundaries. Misorientation was used to highlight the high strain [18] whilst elsewhere, variations in local misorientation have been said to be indicative of lattice strain [19]. In this case, the lack of indexing may suggest a microstructural difference between specimens. Such difficulties with obtaining indexed diffraction patterns were commented on by Wright et al. [20] for



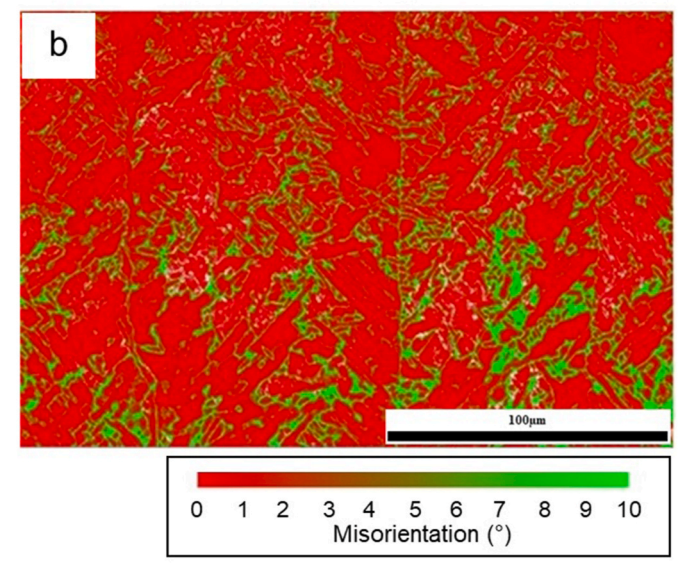


Fig. 9. Local misorientation map for a) Sample 5; low energy density ($E_0^* = 3.80$) and b) Sample 11; high energy density specimen ($E_0^* = 9.55$). The green end of the colour spectrum indicates a higher local misorientations (°). (For interpretation of the references to colour in this figure legend, the reader is referred to the Web version of this article.)

materials subjected to higher stress. However, one of the most common causes is due to specimen preparation. Despite this, the same preparation methods have been used for both the larger and smaller grained variant and therefore is suggestive of a greater residual stress in the material because of a reduced energy input.

4. Conclusions

In this study, an in-depth microstructural analysis of a series of EBM Ti-6Al-4V components has been undertaken and compared to some of the most fundamental parameters from the normalised process map, assessing what has been considered and predicted to be an acceptable process window. Advanced microscopic methods have been utilised and the following conclusions have been drawn.

 Powdered Ti-6Al-4V has been additively manufactured using an Arcam S12 EBM platform using manual input parameters which over-ride standard melt themes to produce two batches of cubic structures. Each batch of cubes were produced with differing beam current values modulated with different input power settings and

- proportional beam speed modifications to ensure that each batch is manufactured with equal energy density values.
- Multiple specimens were manufactured using the same parameter sets within a given build run. The resulting similarity in the microstructure between each cube demonstrated the insensitivity of the microstructure in terms of baseplate location.
- 3. Lower energy density specimens produced a refined α lath structure with a greater degree of discontinuous β rod formations with an average α lath width of 0.97 μm . A higher energy density led to microstructural coarsening with an average α lath width of 1.86 μm . Such coarsening was observed in the colony size and prior- β columnar grain size and were found to follow a logarithmic trend. Increased energy density also promoted an increase in colony size and hence effective structural units which has the effect of increasing local texture.
- 4. No apparent anomalies, such as lack of fusion features or porosity, were reported in the material suggesting the parameter window is suitable for component trials. However, because the size increases relatively proportionally across the scale, a single feature such as the lath measurement could be effectively used to correlate to mechanical properties without the need for colony or columnar width measurements.
- 5. Electron backscatter diffraction analysis was performed on a representative low-energy density specimen and on a high-energy density specimen. Clear differences in overall texture between the two specimens are observed, with maximum multiples of uniform density increasing from $\sim\!19$ in the low-energy density specimen to $\sim\!51$ in the case of the high-energy density condition.

Declaration of competing interest

The authors declare the following financial interests/personal relationships which may be considered as potential competing interests: Robert J Lancaster reports financial support was provided by Rolls-Royce plc. Meurig Thomas reports financial support was provided by Rolls-Royce plc and Innovate UK. Gareth Davies reports financial support was provided by the Engineering and Physical Sciences Research Council (EPSRC) and Rolls-Royce plc. Iain Todd reports financial support was provided by Innovate UK. If there are other authors, they declare that they have no known competing financial interests or personal relationships that could have appeared to influence the work reported in this paper.

Acknowledgements

The current research was funded under the EPSRC Rolls-Royce Strategic Partnership in Structural Metallic Systems for Gas Turbines (grants EP/H500383/1 and EP/H022309/1). The provision of materials and supporting information from Rolls-Royce plc is gratefully

acknowledged. MT and IT would also like to acknowledge Innovate UK for providing additional financial support to this project (grant TSB 52928-379233).

References

- [1] Chern AH, Nandwana P, Yuan T, Kirka MM, Dehoff RR, Liaw PK, et al. A review on the fatigue behavior of Ti-6Al-4V fabricated by electron beam melting additive manufacturing. Int J Fatig 2019;119:173–84.
- [2] Nguyen HD, Pramanik A, Basak AK, Dong Y, Prakash C, Debnath S, et al. A critical review on additive manufacturing of Ti-6Al-4V alloy: microstructure and mechanical properties. J Mater Res Technol 2022;18:4641–61.
- [3] Juechter V, Scharowsky T, Singer RF, Körner C. Processing window and evaporation phenomena for Ti-6Al-4V produced by selective electron beam melting. Acta Mater 2014;76:252–8.
- [4] Reijonen J. The effect of focal point parameters in fiber laser welding of structural steel [PhD thesis]. Lappeenranta University of Technology; 2015.
- [5] Körner C, Attar E, Heinl P. Mesoscopic simulation of selective beam melting processes. J Mater Process Technol 2011;211(6):978–87.
- [6] Rausch AM, Küng VE, Pobel C, Markl M, Körner C. Predictive simulation of process windows for powder bed fusion additive manufacturing: influence of the powder bulk density. Materials 2017;10(10):1117.
- [7] Morita T, Tsuda C, Nakano T. Influences of scanning speed and short-time heat treatment on fundamental properties of Ti-6Al-4V alloy produced by EBM method. Mater Sci Eng 2017;704:246-51.
- [8] Narra SP, Cunningham R, Beuth J, Rollett AD. Location specific solidification microstructure control in electron beam melting of Ti-6Al-4V. Addit Manuf 2018; 19:160-6.
- [9] Kirchner A, Klöden B, Luft J, Weißgärber T, Kieback B. Process window for electron beam melting of Ti-6Al-4V. Powder Metallurgy. 2015 2015;58(4):246–9.
- [10] Thomas M, Baxter GJ, Todd I. Normalised model-based processing diagrams for additive layer manufacture of engineering alloys. Acta Mater 2016;108:26–35.
- [11] Keist J, Palmer T. Development of strength-hardness relationships in additively manufactured titanium alloys. Mater Sci Eng. A 2017;693:214–24.
- [12] Vrancken B, Thijs L, Kruth JP, Van Humbeeck J. Heat treatment of Ti6Al4V produced by selective laser melting: microstructure and mechanical properties. J Alloys Compd 2012;541:177–85.
- [13] Ednie L, Antonysamy AA, Parimi L, Mani M, Thomas M, Lancaster RJ. Understanding the fatigue behaviour of Ti–6Al–4V manufactured via various additive processes. J Mater Res Technol 2024;31:1337–54.
- [14] Galarraga H, Warren RJ, Lados DA, Dehoff RR, Kirka MM, Nandwana P. Effects of heat treatments on microstructure and properties of Ti-6Al-4V ELI alloy fabricated by electron beam melting (EBM). Mater Sci Eng 2017;685:417–28.
- [15] Antonysamy AA. Microstructure, texture and mechanical property evolution during additive manufacturing of Ti6Al4V alloy for aerospace applications [PhD thesis]. University of Manchester; 2012.
- [16] Sackett E, Germain L, Bache M. Crystal plasticity, fatigue crack initiation and fatigue performance of advanced titanium alloys. Int J Fatig 2017;29:2015–21.
- [17] Brewer L, Othon MA, Young LM, Angeliu TM. Misorientation mapping for visualisation of plastic strain via electron back-scattered diffraction. Microsc Microanal 2006;12(1):85–91.
- [18] Salvati E, O'Connor S, Nowell D, Korsunsky A. EBSD investigation of fatigue crack propagation past a crack closure due to overload. In: Proceedings of the 5th international conference on crack paths (CP 2015). Italy: Ferrara; 2015. Sept 16-18.
- [19] Albiston BM. Influence of microstructure on the propagation of fatigue cracks in inconel 617 [PhD thesis]. Boise State University; 2013.
- [20] Wright SI, Nowell MM, Lindeman SP, Camus PP, De Graef M, Jackson MA. Introduction and comparison of new EBSD post-processing methodologies. Ultramicroscopy 2015;159:81–94.